# Recoil polarization observables in the electroproduction of $K$ mesons and $\Lambda$'s from the proton

Oren V. Maxwell
*Department of Physics, Florida International University, Miami, Florida 33199, USA*
(Received 1 July 2014; published 8 September 2014)

A model developed previously to investigate the electromagnetic production of strangeness from the proton is used to investigate single and double recoil polarization observables in the reaction $ep \to e'K^+\Lambda$ in the relativistic impulse approximation. The formalism is based on a tree-level, effective Lagrangian model, which incorporates a variety of baryon resonances with spins up to $\frac{5}{2}$ and the two kaon resonances, $K^\star(892)$ and $K1(1270)$. The parameters of the model were fit to a large pool of photoproduction data from the CLAS, GRAAL, SAPHIR, and LEPS collaborations and to CLAS data for the virtual photoproduction structure functions $\sigma_U$, $\sigma_T$, $\sigma_L$, $\sigma_{TT}$, $\sigma_{LT}$, and $\sigma_{LT'}$. Using two different versions of this model, results are presented for three recoil polarization asymmetries that have been measured recently at CLAS. A new fit is then presented which incorporates the new polarization data in the fitted data set. Results obtained with this new fit are presented for six recoil polarization asymmetries and compared with results from one of the previous fits.

DOI: 10.1103/PhysRevC.90.034605 PACS number(s): 24.10.Jv, 25.10.+s, 25.30.Rw, 13.60.−r

## I. INTRODUCTION

The electromagnetic production of kaons from the proton has received a considerable amount of attention over the past couple of decades. Initially, interest focused on the photoproduction reaction, but in later years, the electroproduction reaction has received an increasing share of both the theoretical and experimental effort in this field. Recently, the CEBAF group extended the pool of electroproduction data to include data for the transferred beam-recoil polarization asymmetries, $P'_x$ and $P'_z$ [1], and for the induced polarization asymmetry, $P^0_y$ [2]. Such data provide additional constraints on theoretical models for electromagnetic strangeness production and narrow the constraints on baryonic resonance models.

Electroproduction of strangeness from the proton was first examined in the mid 1970's using a simple Regge model [3]. More recent theoretical studies have been based on a variety of approaches, including effective Lagrangian models [4–10], Regge models [11], and chiral models [12,13]. The work discussed here is based on a pair of fits reported in Ref. [14]. These fits were obtained from an effective Lagrangian model developed earlier in Ref. [15] that incorporates most of the well-established baryon resonances with spins up to $\frac{5}{2}$, four less well-established nucleon resonances of higher mass, and the two kaon resonances, $K^\star(892)$ and $K1(1270)$. To account for the off-shell nature of the virtual photon in electroproduction, the model employs phenomenological form factors at the hadron electromagnetic vertices. The parameters of the model were fit to photoproduction data from the CLAS [16–18], SAPHIR [19], LEPS [20], and GRAAL [21,22] collaborations and to electroproduction data from CLAS [23,24].

A summary of the underlying reaction model is presented in the next section. For a more complete description, the reader should consult Refs. [14,15]. The formalism associated with the recoil polarization observables is discussed in Sec. III. These observables are defined through a general expression for the virtual photoproduction cross section and then expressed explicitly in terms of a set of structure functions, which depend on the particular coordinate system employed. Calculated results for the polarization observables, obtained with the two fits presented in Ref. [14], are discussed and compared with the data in Sec. IV. A new fit based on the same model, but with the recoil polarization observables included in the fitted data set, is presented in Sec. V. This section includes results for all six of the polarization asymmetries defined in Sec. III and a comparison of those results with results from one of the previous fits. Finally, Sec. VI contains a summary of the results and conclusions.

## II. VIRTUAL PHOTOPRODUCTION MODEL

The electroproduction reaction model employed in this work is based on a single photon exchange approximation in which the electroproduction matrix element is expressed as the contraction of a lepton current matrix element with a hadron current matrix element multiplied by the propagator of the intermediate virtual photon. The lepton matrix element has a standard form given by QED, while the hadron matrix element has the general form

$$h^\mu = e\bar{u}_{M_\Lambda}(p_\Lambda)\hat{t}^\mu u_{M_p}(p_p). \tag{1}$$

The amplitude appearing in this matrix element has contributions of three different types, represented diagrammatically in Fig. 1. These three types of contributions are generally labeled $s$-channel, $u$-channel, or $t$-channel contributions, in accordance with the Mandelstaam variable that appears in the propagator of the intermediate hadron. In each channel, the Born contributions are supplemented by nucleon resonances ($s$-channel), hyperon resonances ($u$-channel), or kaon resonances ($t$-channel). A list of all the resonances included in the model can be found in Ref. [14].

 

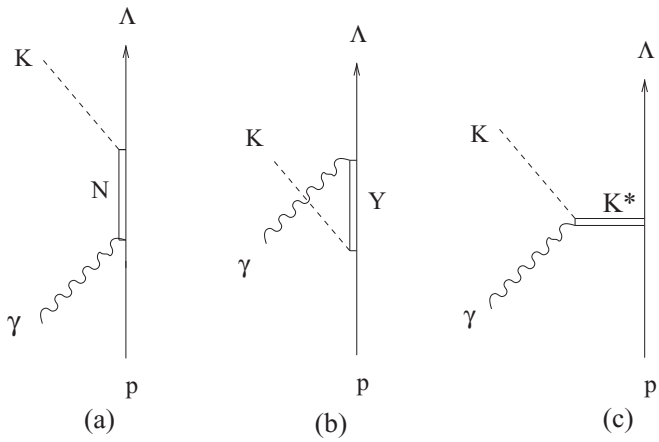


FIG. 1. Contributions to the amplitude for the reaction $\gamma p \to K^+\Lambda$ in the (a) $s$ channel, (b) $u$ channel, and (c) $t$ channel.

The amplitudes associated with these various contributions have the general structures

$$\hat{t}_s^\mu = \sum_{N^\star} [\mathcal{V}_K^\dagger(p_K) D(p_s) \mathcal{V}_\gamma(q)]^\mu,$$
$$\hat{t}_u^\mu = \sum_{Y^\star} [\mathcal{V}_\gamma^\dagger(q) D(p_u) \mathcal{V}_K(p_K)]^\mu, \quad (2)$$
$$\hat{t}_t^\mu = \sum_{K^\star} [\mathcal{V}_{\gamma K}^\dagger(q, p_t) D_t(p_t) \mathcal{V}_{p\Lambda}(p_t)]^\mu,$$

where the $\mathcal{V}$'s designate the interaction vertices and the $D$'s the intermediate hadron propagators. The quantities $p_s = p_\Lambda + p_K$, $p_u = p_\Lambda - q$, and $p_t = q - p_K$ are the four-momenta transferred in the $s$, $u$, and $t$ channels respectively.

The interaction vertices and propagators in these expression depend on the spins and parities of the intermediate hadrons. The interaction vertices are discussed in some detail in Refs. [14,15]. For the spin-$\frac{1}{2}$ propagator, a relativistic Breit-Wigner form is used with an energy- and momentum-dependent width included in the $s$-channel resonance contributions. The spin-$\frac{3}{2}$ and spin-$\frac{5}{2}$ resonances are generated from the spin-$\frac{1}{2}$ propagator by appending the appropriate spin projection operators. In the $t$ channel, the standard spin-0 propagator is employed for the kaon. This is multiplied by the spin-1 projection operator to obtain the spin-1 propagator appropriate for the kaon resonances. Explicit expressions for all the interaction vertices and propagators employed in the model are given in Ref. [14].

The resonance decay widths required in the $s$-channel propagators are obtained from a dynamical model that generates the energy and momentum dependences in various decay channels using an effective Lagrangian. The normalizations of the partial widths are fixed on shell using empirical branching ratio data. Details can be found in Ref. [25].

To take account of the off-shell nature of the virtual photons in electroproduction, form factors have been included in the electromagnetic vertex functions. The inclusion of form factors in the Born contributions also requires the addition of counterterms to preserve gauge invariance. Both the form factors employed and the necessary counterterms are discussed in detail in Ref. [15].

The fitted data included a large set of photoproduction data from CLAS, SAPHIR, LEPS, and GRAAL plus electroproduction data from CLAS. The data were fit in a two-step iterative procedure. In the first step the form factor parameters were fixed and the products of the coupling strengths at the two interaction vertices of each contribution were varied. Only the resonance couplings were treated as fitted parameters. The Born couplings were fixed by a combination of empirical data and symmetry considerations, as discussed in Ref. [15]. In the second step, the couplings were fixed, and the mass and coupling parameters associated with the electromagnetic form factors were varied. In each step of the procedure, the $\chi^2$ per degree of freedom was minimized. The degree of convergence of the procedure was assessed by comparing the $\chi^2$ values obtained in successive iterations. In practice it was found that the procedure converges quite well after only two iterations.

Two different fits were obtained by this procedure. The two fits differ in the set of nucleon resonances that was incorporated in the fit. In the first fit, labeled here fit A, the lower-energy nucleon resonances of four star status in the particle data tables were supplemented by four less well-established resonances of higher energy. In a later version of the particle data tables, two of these higher-energy resonances, $N(2080)$ and $N(2200)$, were expunged from the tables. The second fit of Ref. [14], labeled here fit B, does not include these two resonances. Tables of parameter values for these two fits can be found in Ref. [14].

## III. POLARIZATION OBSERVABLES

To define the polarization observables in electroproduction from the proton, it is convenient to work in the center of mass (c.m.) frame of the virtual photon and the proton target. In this frame for an experiment in which the polarizations of the incident electron and the outgoing hyperon are measured, the differential virtual photoproduction cross section has the general structure

$$\frac{d\sigma_\gamma}{d\Omega_K} = \sigma_0[1 + \mathcal{H}A_{LT'} + P_x S_x + P_y S_y + P_z S_z], \quad (3)$$

where $\sigma_0$ is the unpolarized differential cross section, $\mathcal{H}$ is the electron helicity, $A_{LT'}$ is the electron beam asymmetry, the $S$'s are components of the spin projection operator defined with respect to the hadron plane, and the $P$'s are the corresponding hyperon polarization asymmetries. Each of the last quantities can be expressed as the sum of a term independent of the electron helicity, the induced polarization asymmetry, and a helicity-dependent part, the transferred polarization asymmetry. In particular,

$$P_i = P_i^0 + \mathcal{H}P_i' \quad (4)$$

for $i = x$, $y$, or $z$.

The dependences of the various induced and transferred polarization asymmetries on $\epsilon$, the transverse photon polarization, and $\phi$, the angle between the electron and hadron planes, can be made explicit through the introduction of a set of polarization structure functions. In terms of these structure

functions, the polarization asymmetries are given by

$$\begin{aligned}
\sigma_0 P_x^0 &= K \sum_{M_p} \left[\epsilon R_{TT}^x \sin 2\phi + c_+ R_{LT}^x \sin\phi\right],\\
\sigma_0 P_x' &= K \sum_{M_p} \left[\sqrt{1-\epsilon^2} R_{TT'}^x + c_- R_{LT'}^x \cos\phi\right],\\
\sigma_0 P_y^0 &= K \sum_{M_p} \left[R_T^y + \epsilon \frac{-q^2}{q_0^2} R_L^y + \epsilon R_{TT}^y \cos 2\phi \right.\\
&\qquad \left. + c_+ R_{LT}^y \cos\phi\right], \qquad (5)\\
\sigma_0 P_y' &= K \sum_{M_p} \left[c_- R_{LT'}^y \sin\phi\right],\\
\sigma_0 P_z^0 &= K \sum_{M_p} \left[\epsilon R_{TT}^z \sin 2\phi + c_+ R_{LT}^z \sin\phi\right],\\
\sigma_0 P_z' &= K \sum_{M_p} \left[\sqrt{1-\epsilon^2} R_{TT'}^z + c_- R_{LT'}^z \cos\phi\right],
\end{aligned}$$

with

$$K = \frac{m_P m_\Lambda p_K}{16\pi^2 |\mathbf{q}| s} \qquad (6)$$

and

$$c_\pm = \frac{\sqrt{-2q^2\epsilon(1\pm\epsilon)}}{q_0}, \qquad (7)$$

where $q^2$ is the square of the virtual photon four-momentum, $\mathbf{q}$ is the virtual photon three-momentum, and $s$ is the square of the virtual photon-proton c.m. energy.

The connections between the polarization structure functions and the hadron matrix elements defined previously depend on the choice of coordinate axes. Choosing the $z$ axis along the virtual photon direction and the $x$ axis in the hadron plane so that the $x$ component of the outgoing kaon momentum is positive yields the relations

$$\begin{aligned}
R_{TT}^x &= -\frac{1}{2}(h_x^\star h_y + h_y^\star h_x)_{+-},\\
R_{LT}^x &= \frac{1}{2}(h_z^\star h_y + h_y^\star h_z)_{+-},\\
R_{TT'}^x &= \frac{i}{2}(h_x^\star h_y - h_y^\star h_x)_{+-},\\
R_{LT'}^x &= -\frac{i}{2}(h_z^\star h_y - h_y^\star h_z)_{+-},\\
R_T^y &= -\frac{i}{2}(h_x^\star h_x + h_y^\star h_y)_{+-},\\
R_L^y &= -i(h_z^\star h_z)_{+-},\\
R_{TT}^y &= -\frac{i}{2}(h_x^\star h_x - h_y^\star h_y)_{+-},\\
R_{LT}^y &= \frac{i}{2}(h_x^\star h_z + h_z^\star h_x)_{+-},\\
R_{LT'}^y &= \frac{1}{2}(h_x^\star h_z - h_z^\star h_x)_{+-},\\
R_{TT}^z &= -\frac{1}{2}(h_x^\star h_y + h_y^\star h_x)_{++},\\
R_{LT}^z &= \frac{1}{2}(h_z^\star h_y + h_y^\star h_z)_{++},\\
R_{TT'}^z &= \frac{i}{2}(h_x^\star h_y - h_y^\star h_x)_{++},\\
R_{LT'}^z &= -\frac{i}{2}(h_z^\star h_y - h_y^\star h_z)_{++}, \qquad (8)
\end{aligned}$$

where the $+-$ subscripts specify the $\Lambda$ spin projections in the hadron matrix elements; for example, the subscript $+-$ specifies that the first matrix element in the product is to evaluated with $M_\Lambda = +\frac{1}{2}$ and the second with $M_\Lambda = -\frac{1}{2}$. Note that the structure functions are all defined so that they are real.

The hadron plane coordinate system employed in the CLAS measurements has the $z$ axis pointing in the direction of the outgoing kaon momentum, rather than in the direction of the virtual photon. The corresponding polarization asymmetries are related to the ones defined above by a simple rotation around the y-axis of the original coordinate system. One obtains

$$\begin{aligned}
\hat{P}_x &= P_x \cos\theta_K - P_z \sin\theta_K,\\
\hat{P}_y &= P_y, \qquad (9)\\
\hat{P}_z &= P_x \sin\theta_K + P_z \cos\theta_K,
\end{aligned}$$

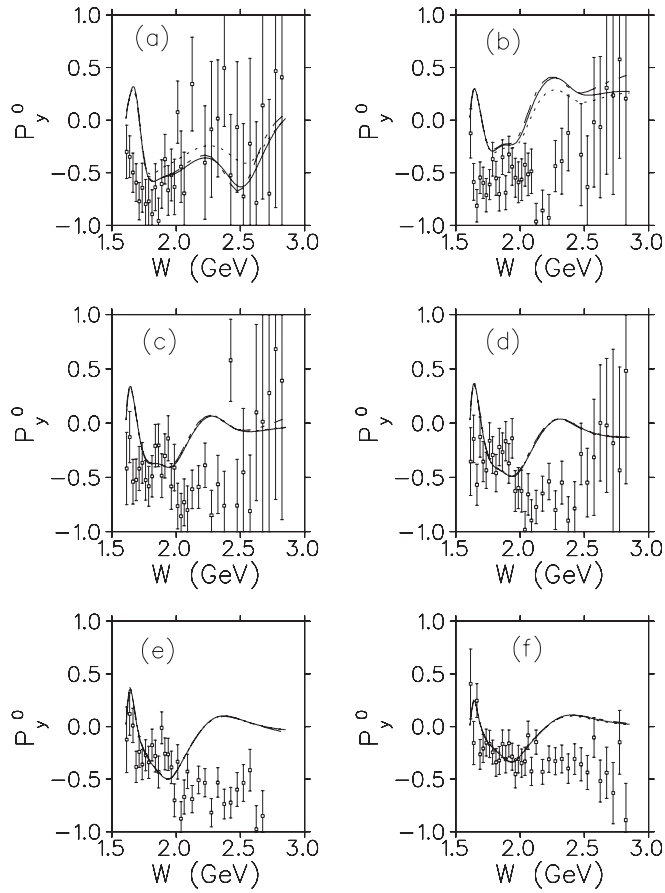


FIG. 2. $P_y^0$ vs $W$ for $E_{\rm Lab} = 5.499$ GeV, and (a) $\cos\theta_K = -0.725$, (b) $\cos\theta_K = -0.217$, (c) $\cos\theta_K = 0.106$, (d) $\cos\theta_K = 0.305$, (e) $\cos\theta_K = 0.706$, (f) $\cos\theta_K = 0.910$. In each panel, the solid, dot-dashed, and dotted curves were obtained as explained in the text. All curves have been averaged over the angle $\phi$ and were obtained using the fit B described in the text. Data are from Ref. [2].

where the polarization asymmetries on the left are the rotated ones, and the polarization asymmetries on the right are the ones defined by Eq. (4).

To achieve reasonable statistics, it was necessary to average the polarization measurements over the angle $\phi$. This causes all the terms in Eqs. (5) involving sines and cosines of $\phi$ or $2\phi$ to vanish, so that Eqs. (5) reduce to

$$\begin{aligned}
\sigma_0 P_x^0 &= 0, \\
\sigma_0 P_x' &= K \sum_{M_p} \sqrt{1-\epsilon^2} R_{TT'}^x, \\
\sigma_0 P_y^0 &= K \sum_{M_p} \left[ R_T^y + \epsilon \frac{-q^2}{q_0^2} R_L^y \right], \\
\sigma_0 P_y' &= 0, \\
\sigma_0 P_z^0 &= 0, \\
\sigma_0 P_z' &= K \sum_{M_p} \sqrt{1-\epsilon^2} R_{TT'}^z.
\end{aligned} \tag{10}$$

## IV. RESULTS

In this section we report results for the induced polarization asymmetry $P_y^0$ and the transferred polarization asymmetries $P_x'$ and $P_z'$ obtained with the fits A and B described above. As noted previously, these two fits incorporate electron beam asymmetry data but no other polarization data. All of the results reported in this section have been averaged over the angle $\phi$ between the electron and hadron planes unless otherwise noted.

The CLAS data for the induced polarization asymmetry are more extensive than for the transferred polarization asymmetries, so we first focus on the observable $P_y^0$. To achieve reasonable statistics, it was necessary in the CLAS experiment to employ rather large kinematic bins, particularly in $q^2$ and $\cos\theta_K$. Moreover, the bin sizes depend on the particular kinematic point considered. The $\cos\theta_K$ bins, for example, are much larger at backward angles than forward angles. There are also correlations between the bins for different kinematic variables. For example, the central values of the $q^2$ bins depend on $W$. For all of these reasons, some care must be exercised in comparing calculated results, which are typically obtained for single kinematic points, with empirical results, which

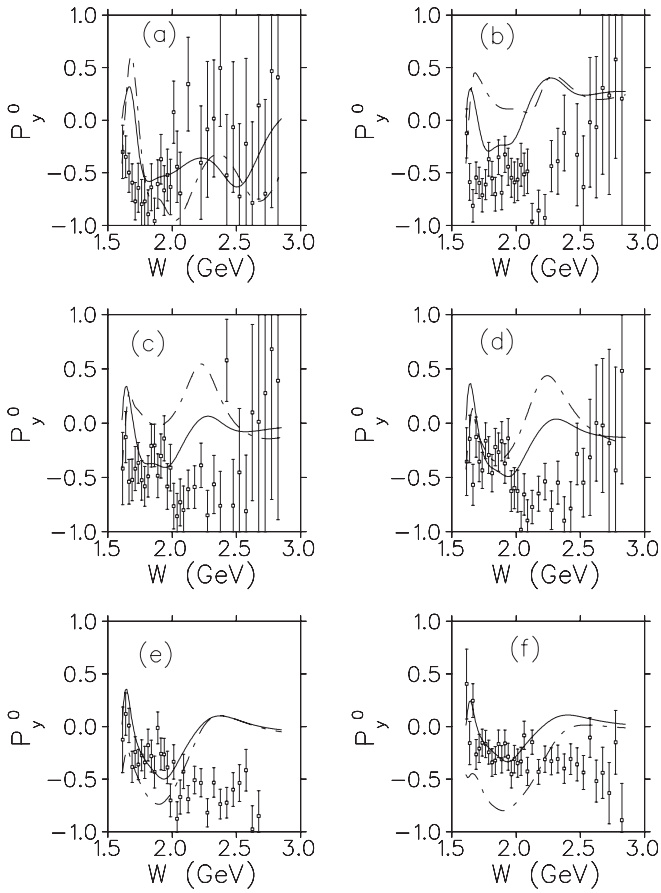


FIG. 3. $P_y^0$ vs $W$ for $E_{\rm Lab} = 5.499$ GeV, $-q^2 = 1.90$ GeV$^2$, and (a) $\cos\theta_K = -0.725$, (b) $\cos\theta_K = -0.217$, (c) $\cos\theta_K = 0.106$, (d) $\cos\theta_K = 0.305$, (e) $\cos\theta_K = 0.706$, (f) $\cos\theta_K = 0.910$. In each panel, the solid curve has been averaged over the angle $\phi$, while the dash-dotted curve was obtained with $\phi = 30^\circ$. Both curves were obtained with the fit B described in the text. Data are from Ref. [2].

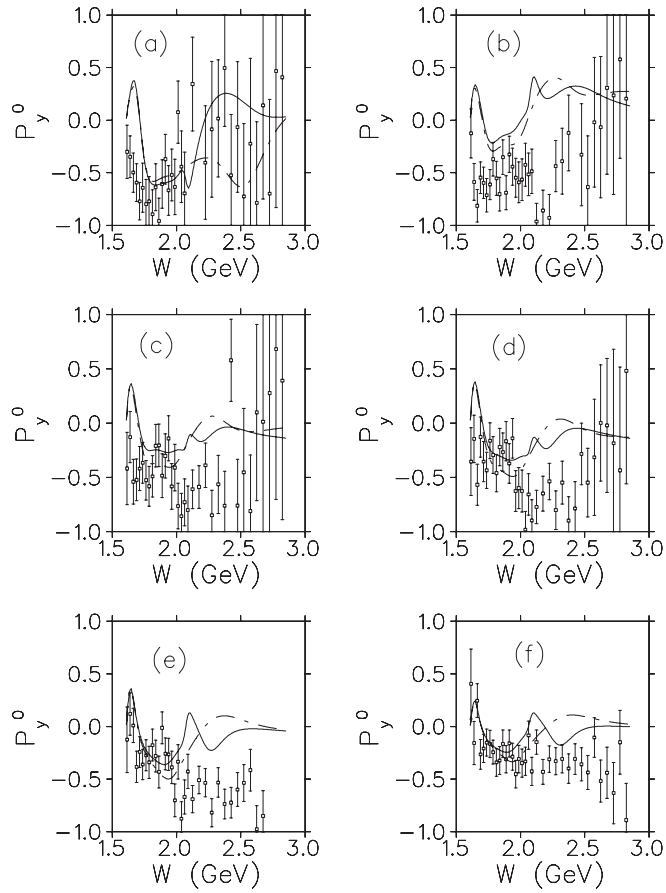


FIG. 4. $P_y^0$ vs $W$ for $E_{\rm Lab} = 5.499$ GeV, $-q^2 = 1.90$ GeV$^2$, and (a) $\cos\theta_K = -0.725$, (b) $\cos\theta_K = -0.217$, (c) $\cos\theta_K = 0.106$, (d) $\cos\theta_K = 0.305$, (e) $\cos\theta_K = 0.706$, (f) $\cos\theta_K = 0.910$. In each panel, the solid curve was obtained with fit A and the dash-dotted curve with fit B as described in the text. All curves have been averaged over the angle $\phi$ as described in the text. Data are from Ref. [2].

represent averages over a multidimensional kinematic range around the quoted point.

Some of these issues are explored in Fig. 2. In this figure, results for $P_y^0$ using fit B are shown as functions of $W$ for several values of $\cos\theta_K$. The solid curves were all obtained with a single average value $-q^2 = 1.90\ \mathrm{GeV}^2$. To obtain the dot-dashed curves, the $-q^2$ value for each $W$ was set equal to the cross section weighted center of the $-q^2$ bin corresponding to that $W$ value. Finally, the dotted curve for each $\cos\theta_K$ represents a cross section weighted average over the entire angle bin which has that value of $\cos\theta_K$ as its cross section weighted central value.

As can be seen in the figure, the curves in each panel generally coincide to a remarkable degree. The only significant differences appear at the two back angles where the dotted curves diverge somewhat from the other two. The coincidence of the solid and dash-dotted curves reflects the relatively weak $q^2$ dependence of this observable over the kinematic range considered. This lack of $q^2$ dependence, which is shown more explicitly in a later figure, justifies the use of a single average $-q^2$ value to study the the energy dependence of $P_y^0$. The coincidence of the solid and dotted curves in most of the panels indicates that differences between empirical and calculated values of $P_y^0$ cannot be attributed to the finite-sized angle bins in the CLAS experiments. The fact that there is some difference between the solid and dotted curves at back angles probably reflects the especially large bin sizes at those central angle values.

Comparison with the data for this observable yields mixed conclusions. At lower energies, the model generally reflects the trend in the data, although the calculated values lie a bit too high at the back angles. At higher energies and forward angles, the measured observable becomes more negative, while the model predicts values near zero. At higher energies and back angles, the size of the error bars precludes a meaningful comparison between the the model results and the data.

The effect of averaging over the angle $\phi$ is explored in Fig. 3. This figure again exhibits results for $P_y^0$ as a function of $W$ using fit B. The solid curves in this figure are the same as in the previous figure; they were obtained by averaging over $\phi$. The dot-dashed curves were obtained with the specific choice $\phi = 30^\circ$. One can see here that the calculated results for $P_y^0$ depend much more on $\phi$ than they do on $-q^2$ or the method of

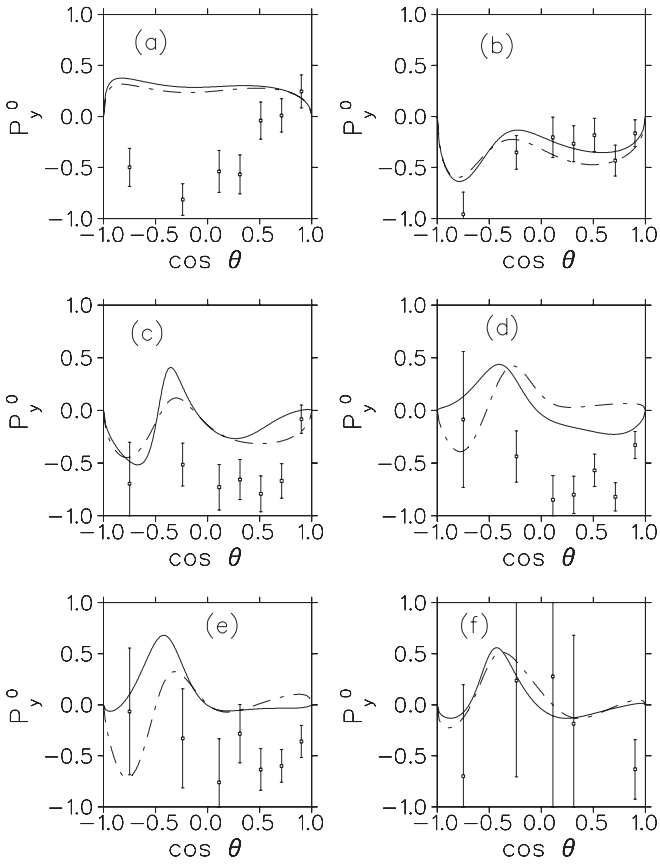


FIG. 5. $P_y^0$ vs $\cos\theta_K$ for $E_{\mathrm{Lab}} = 5.499\,\mathrm{GeV}$ and (a) $W = 1.633\,\mathrm{GeV}$, $-q^2 = 2.11\ \mathrm{GeV}^2$, (b) $W = 1.863\,\mathrm{GeV}$, $-q^2 = 2.08\ \mathrm{GeV}^2$,(c) $W = 2.063\,\mathrm{GeV}$, $-q^2 = 2.01\ \mathrm{GeV}^2$, (d) $W = 2.274\,\mathrm{GeV}$, $-q^2 = 1.90\ \mathrm{GeV}^2$, (e) $W = 2.475\,\mathrm{GeV}$, $-q^2 = 1.75\ \mathrm{GeV}^2$, (f) $W = 2.724\,\mathrm{GeV}$, $-q^2 = 1.52\ \mathrm{GeV}^2$. In each panel, the solid curve was obtained with fit A and the dash-dotted curve with fit B as described in the text. All curves have been averaged over the angle $\phi$ as described in the text. Data are from Ref. [2].

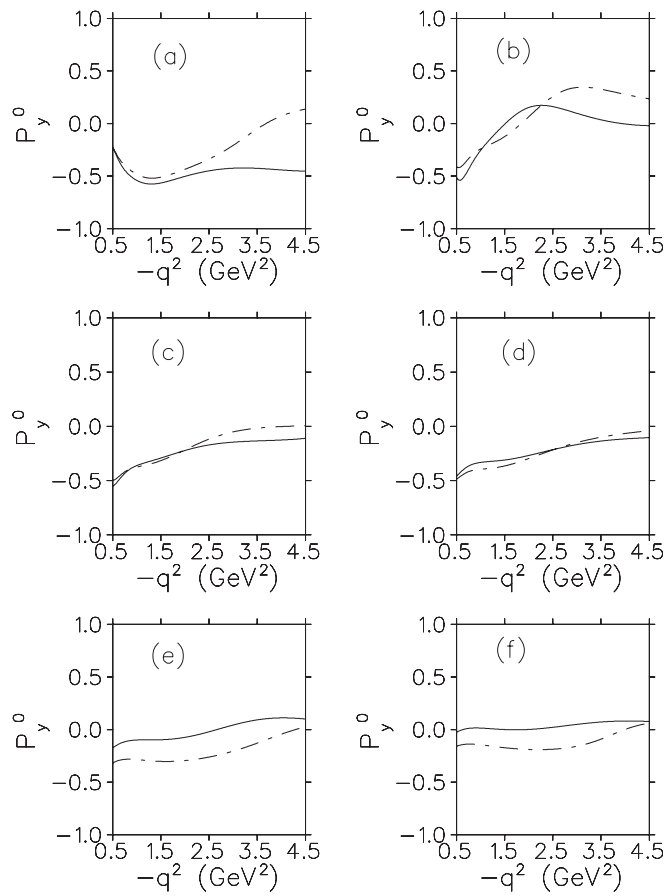


FIG. 6. $P_y^0$ vs $-q^2$ for $E_{\mathrm{Lab}} = 5.499\,\mathrm{GeV}$, $W = 2.0625\,\mathrm{GeV}$, and (a) $\cos\theta_K = -0.725$, (b) $\cos\theta_K = -0.217$, (c) $\cos\theta_K = 0.106$, (d) $\cos\theta_K = 0.305$, (e) $\cos\theta_K = 0.706$, (f) $\cos\theta_K = 0.910$. In each panel, the solid curve was obtained with fit A and the dash-dotted curve with fit B as described in the text. All curves have been averaged over the angle $\phi$ as described in the text.

treating finite bin sizes. This is not surprising since, as seen in Eq. (10), three of the polarization asymmetries actually vanish when averaged over $\phi$.

Figure 4 exhibits the energy dependence of $P_y^0$ for the two different fits discussed previously. The solid curves in this figure were obtained with fit A, while the dot-dashed curves were obtained with fit B. Since the two fits employed the same data and are of comparable quality, it is interesting that they yield somewhat different results for $P_y^0$. One feature in particular that is noteworthy is the bump around $W = 2.1$GeV that appears in the fit A results but not in the fit B results. Such differences indicate that in the future, measurements of $P_y^0$ may be able to provide significant new constraints on effective Lagrangian descriptions of strangeness production. Unfortunately, with the statistics currently achievable, no conclusions can be yet drawn as to the relative merits of the two fits

Angular distributions obtained with the two fits are exhibited in Fig. 5. As in the previous figure, the solid curves were obtained with fit A, the dashed curves with fit B. There are differences in the two sets of results, which are energy dependent, but again the quality of the data does not permit us to draw any conclusions as to which fit is superior.

Figure 6 shows the $q^2$ dependence of the calculated $P_y^0$ for both fits. As mentioned earlier, the calculated $P_y^0$ depends rather weakly on $q^2$ over the whole kinematic range considered. This conclusion is clearly reinforced by the results displayed in this figure. Once again, there are differences in the results obtained from the two fits, but except at the lowest energy, these differences are less significant than those evident in the previous figures.

The remaining two figures in this section exhibit results for the transferred polarization asymmetries $P_x'$ and $P_z'$ with the $P_z'$ results shown on the left in each figure and the $P_x'$ results on the right. The solid curves in both figures were obtained with fit A, the dot-dashed curves with fit B.

Figure 7 displays angular distributions for the two polarization observables for three different choices of $W$ and $-q^2$. In general, the differences between the two fits are smaller than for the induced polarization asymmetry. As for $P_y^0$, comparison with the data yields mixed conclusions. In

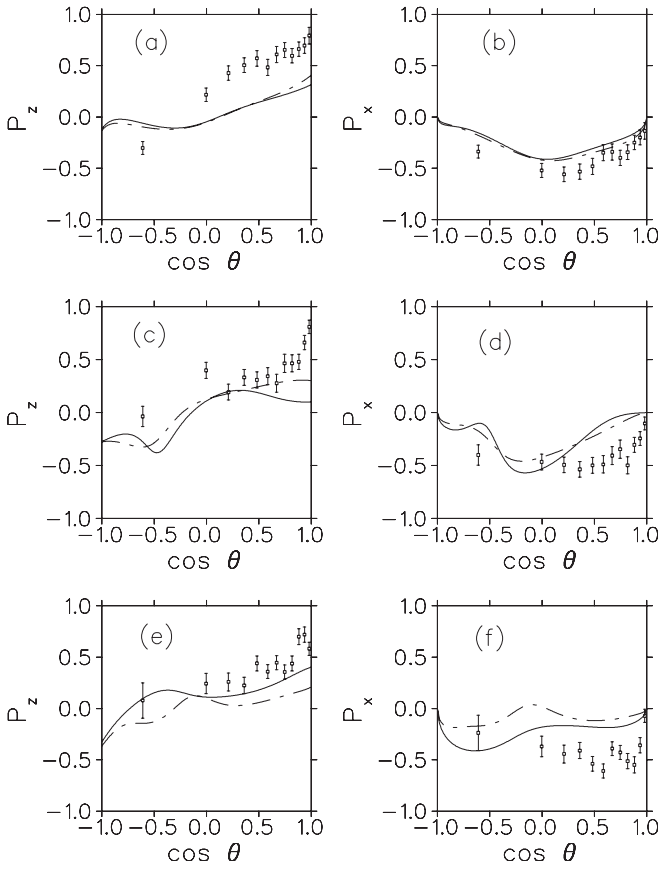


FIG. 7. $P_z'$ vs $\cos\theta_K$ for $E_{\rm Lab} = 5.754$ GeV and (a) $W = 1.753$ GeV, $-q^2 = 2.61$ GeV$^2$, (c) $W = 1.985$ GeV, $-q^2 = 2.56$ GeV$^2$, (e) $W = 2.314$ GeV, $-q^2 = 2.41$ GeV$^2$. $P_x'$ vs $\cos\theta_K$ for $E_{\rm Lab} = 5.754$ GeV and (b) $W = 1.753$ GeV, $-q^2 = 2.61$ GeV$^2$, (d) $W = 1.985$ GeV, $-q^2 = 2.56$ GeV$^2$, (f) $W = 2.314$ GeV, $-q^2 = 2.41$ GeV$^2$. In each panel, the solid curve was obtained with fit A and the dash-dotted curve with fit B as described in the text. All curves have been averaged over the angle $\phi$ as described in the text. Data are from Ref. [1].

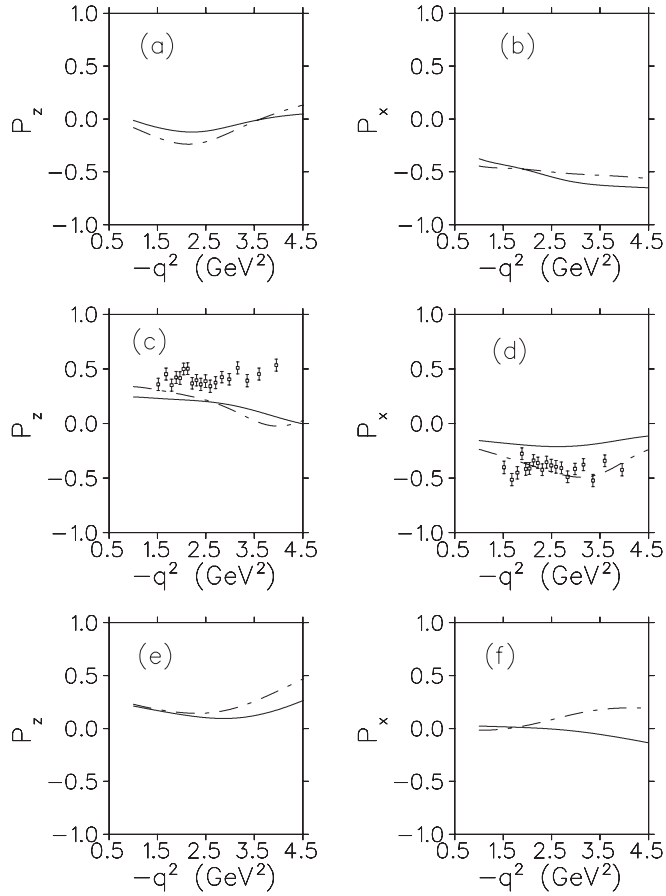


FIG. 8. $P_z'$ vs $-q^2$ for $E_{\rm Lab} = 5.754$ GeV, $W = 1.99$ GeV, and (a) $\cos\theta_K = -0.25$, (c) $\cos\theta_K = 0.43$, (e) $\cos\theta_K = 0.90$. $P_x'$ vs $-q^2$ for $E_{\rm Lab} = 5.754$ GeV, $W = 1.99$ GeV, and (b) $\cos\theta_K = -0.25$, (d) $\cos\theta_K = 0.43$, (f) $\cos\theta_K = 0.90$. In each panel, the solid curve was obtained with fit A and the dash-dotted curve with fit B as described in the text. All curves have been averaged over the angle $\phi$ as described in the text. Data are from Ref. [1].

general, the calculated results show the same trends as the data, but there are discrepancies at particular energies in particular angle ranges.

TABLE I. Fit results for the coupling strength products. For each hadron, the first set of numbers is fit B from Ref. [14] that is described in the text, while the second set is the new fit that includes the polarization observables in the fitted data.

| | | | |
|---|---|---|---|
| | Spin-$\frac{1}{2}$ resonances | | |
| $N(1440)$ | $F_{N^\star}$ | 2.6909 | 2.2903 |
| $N(1535)$ | $F_{N^\star}$ | 0.4267 | 0.3864 |
| $N(1650)$ | $F_{N^\star}$ | −0.0684 | −0.0654 |
| $N(1710)$ | $F_{N^\star}$ | 0.0690 | 0.1096 |
| $\Lambda(1405)$ | $F_{\Lambda^\star}$ | −3.2050 | −3.2854 |
| $\Lambda(1670)$ | $F_{\Lambda^\star}$ | 4.2239 | 4.4372 |
| | Spin-$\frac{3}{2}$ resonances | | |
| $N(1520)$ | $G^1_{N^\star}$ | −0.8292 | −0.9162 |
| | $G^2_{N^\star}$ | −0.3994 | −0.5031 |
| $N(1700)$ | $G^1_{N^\star}$ | −0.0615 | −0.0141 |
| | $G^2_{N^\star}$ | −0.2801 | −0.2061 |
| $N(1720)$ | $G^1_{N^\star}$ | −0.0012 | −0.0009 |
| | $G^2_{N^\star}$ | −0.3815 | −0.4286 |
| $N(1900)$ | $G^1_{N^\star}$ | 0.0359 | 0.0370 |
| | $G^2_{N^\star}$ | 0.0071 | −0.0045 |
| $\Lambda(1890)$ | $G^1_{\Lambda^\star}$ | −1.3007 | −0.8545 |
| | $G^2_{\Lambda^\star}$ | −8.5795 | −9.7806 |
| $\Sigma(1385)$ | $G^1_{\Sigma^\star}$ | −0.1074 | −0.4254 |
| | $G^2_{\Sigma^\star}$ | 6.5442 | 7.2042 |
| $\Sigma(1940)$ | $G^1_{\Sigma^\star}$ | 1.8796 | 1.7369 |
| | $G^2_{\Sigma^\star}$ | 0.3311 | 0.1718 |
| | Spin-$\frac{5}{2}$ resonances | | |
| $N(1675)$ | $G^1_{N^\star}$ | −0.0046 | −0.0044 |
| | $G^2_{N^\star}$ | −0.0126 | −0.0083 |
| $N(1680)$ | $G^1_{N^\star}$ | 0.0274 | 0.0341 |
| | $G^2_{N^\star}$ | 0.0035 | 0.0140 |
| $N(2000)$ | $G^1_{N^\star}$ | −0.0143 | −0.0170 |
| | $G^2_{N^\star}$ | −0.0095 | −0.0135 |
| $\Lambda(1820)$ | $G^1_{\Lambda^\star}$ | −0.1725 | −0.3210 |
| | $G^2_{\Lambda^\star}$ | −1.3133 | −1.0657 |
| $\Lambda(1830)$ | $G^1_{\Lambda^\star}$ | −0.1166 | −0.1209 |
| | $G^2_{\Lambda^\star}$ | −0.3926 | −0.6198 |
| $\Lambda(2110)$ | $G^1_{\Lambda^\star}$ | −0.1560 | −0.2949 |
| | $G^2_{\Lambda^\star}$ | −1.2795 | −1.0909 |
| $\Sigma(1775)$ | $G^1_{\Sigma^\star}$ | 0.1001 | 0.1018 |
| | $G^2_{\Sigma^\star}$ | 0.4068 | 0.6266 |
| $\Sigma(1915)$ | $G^1_{\Sigma^\star}$ | 0.3340 | 0.6132 |
| | $G^2_{\Sigma^\star}$ | 2.5342 | 2.1044 |
| | $t$-Shannel resonances | | |
| $K(892)$ | $G^V_{K^\star}$ | 3.1835 | 3.1308 |
| | $G^T_{K^\star}$ | 1.6769 | 1.6950 |
| $K(1270)$ | $G^V_{K^\star}$ | 1.5024 | 1.4076 |
| | $G^T_{K^\star}$ | −0.9890 | −2.1651 |

The $q^2$ dependence of $P'_x$ and $P'_z$ is exhibited in Fig. 8. As for $P^0_y$, the $q^2$ dependence of both transferred polarization asymmetries is weak, and the differences between the two fits are modest. For the one energy for which data exists, the $P'_x$ results clearly favor fit B.

## V. NEW FIT

In this section we report the results of a new fit to the electromagnetic production of $\Lambda$'s from the proton that includes the recent CLAS polarization data contained in Refs. [1,2]. The fit was performed using the same two-step procedure as was employed in the earlier fits reported in Ref. [14,15]. In the first step of the procedure, the electromagnetic form factors parameters were held fixed while the coupling strength products associated with the resonant contributions to the reaction amplitude were varied. The fitted data in this step included photoproduction data from CLAS [16–18], SAPHIR

TABLE II. Fit results for the electromagnetic form factor parameters. For each hadron, the first set of numbers is fit B from Ref. [14] that is described in the text, while the second set is the new fit that includes the polarization observables in the fitted data.

| | | | | |
|---|---|---|---|---|
| | spin-$\frac{1}{2}$ resonances | | | |
| | $\Lambda$ | $\alpha$ | $\Lambda$ | $\alpha$ |
| $N(1440)$ | 0.3578 | 4.8705 | 1.087 | 4.8705 |
| $N(1535)$ | 1.7029 | 4.5155 | 1.9601 | 4.5155 |
| $N(1650)$ | 4.4379 | −4.8632 | 4.6918 | −4.8632 |
| $N(1710)$ | 4.0544 | 4.0269 | 3.7736 | 4.0269 |
| $F_1(\Lambda)$ | 1.2848 | 4.9737 | 1.1377 | 4.9810 |
| $F_2(\Lambda)$ | 4.9790 | −1.3445 | 4.9790 | −1.2847 |
| $\Lambda(1405)$ | 2.2961 | −0.8464 | 2.5283 | −0.8332 |
| $\Lambda(1670)$ | 0.3368 | −0.1538 | 0.4375 | −0.1065 |
| $\Sigma$ | 1.9300 | −0.9518 | 2.3045 | −0.9525 |
| | Spin-$\frac{3}{2}$ resonances | | | |
| | $\Lambda$ | $\alpha$ | $\Lambda$ | $\alpha$ |
| $N(1520)$ | 1.7450 | 3.4965 | 1.6734 | 3.4965 |
| $N(1700)$ | 2.4139 | −1.4940 | 2.4772 | −1.2700 |
| $N(1720)$ | 1.4104 | 3.7758 | 1.2972 | 3.7758 |
| $N(1900)$ | 4.8314 | −1.2293 | 4.8040 | −1.1623 |
| $\Lambda(1890)$ | 0.3789 | 0.0208 | 0.4000 | −0.0438 |
| $\Sigma(1385)$ | 0.6027 | 4.3992 | 0.5140 | 1.7245 |
| $\Sigma(1940)$ | 0.3449 | 0.1316 | 0.2786 | 2.1796 |
| | Spin-$\frac{5}{2}$ resonances | | | |
| | $\Lambda$ | $\alpha$ | $\Lambda$ | $\alpha$ |
| $N(1675)$ | 1.2417 | 4.8271 | 1.4516 | 1.8549 |
| $N(1680)$ | 1.2080 | 3.2090 | 1.2949 | 2.6037 |
| $N(2000)$ | 1.2272 | 2.7443 | 0.4528 | −0.7264 |
| $\Lambda(1820)$ | 1.0914 | 2.3351 | 1.0711 | 2.0923 |
| $\Lambda(1830)$ | 0.2271 | 3.0470 | 0.2271 | 4.1275 |
| $\Lambda(2110)$ | 0.4831 | −0.4584 | 0.4396 | −0.5195 |
| $\Sigma(1775)$ | 0.3029 | 4.7806 | 0.2263 | 4.4223 |
| $\Sigma(1915)$ | 1.0025 | 1.5652 | 0.9827 | 1.5194 |
| | $t$-channel resonances | | | |
| | $\Lambda_{K^\star}$ | | $\Lambda_{K^\star}$ | |
| $K(892)$ | 0.280 | | 0.207 | |
| $K(1270)$ | 0.921 | | 0.905 | |

[19], LEPS [20], and GRAAL [21,22] and electroproduction data from CLAS [1,2,23,24]. In the second step, the coupling strength products were held fixed and the mass and coupling strength parameters of the electromagnetic form factors were varied. Since the form factors differ from unity only in the electroproduction reaction, only the electroproduction data were incorporated in this step.

In each step of the procedure, the $\chi^2$ per degree of freedom was minimized. This quantity is defined by the expression

$$\chi^2 = \sum \frac{(Y_{\rm calc} - Y_{\rm exp})^2}{\nu \sigma^2}, \tag{11}$$

where the sum is over the data points included in that step, $Y_{\rm calc}$ and $Y_{\rm exp}$ are the calculated and experimental values of the observable, $\sigma^2$ is the squared statistical uncertainty in $Y_{\rm exp}$, and the number of degrees of freedom $\nu$ is the difference between the number of data points and the number of parameters in that step. The procedure was iterated until the $\chi^2$ values obtained in successive iterations no longer changed. In practice, using one of the previous fits as a starting point, this occurred after only two iterations. Further details regarding the fitting procedure, including explicit definitions of the coupling strength products and the form factor parameters, can be found in Ref. [14].

Table I lists the coupling strength products obtained in the new fit along with those obtained in the previous fit B. The corresponding form factor parameters obtained in both fits are listed in Table II. For the most part, the two fits are quite similar. In fact, the parameters of these two fits are less dissimilar than those of the previous fits A and B. There are some differences, for example, in the form factor strengths associated with some of the $\Sigma$ resonances and in the form factors of the $N(2000)$ resonance. The similarities in the fits may be due, in part, to the large error bars accompanying much of the new polarization data, especially the induced polarization asymmetry data, which causes the data to carry less weight in the new fit.

Results obtained with the new fit for the $\phi$ averaged polarization asymmetries are exhibited in the next three figures. In each figure, the solid curves correspond to the new fit, the dash-dotted curves to the previous fit B. The first of these figures, Fig. 9 displays the induced polarization asymmetry as a function of $W$ for the average value $-q^2 = 1.90$ GeV$^2$ and

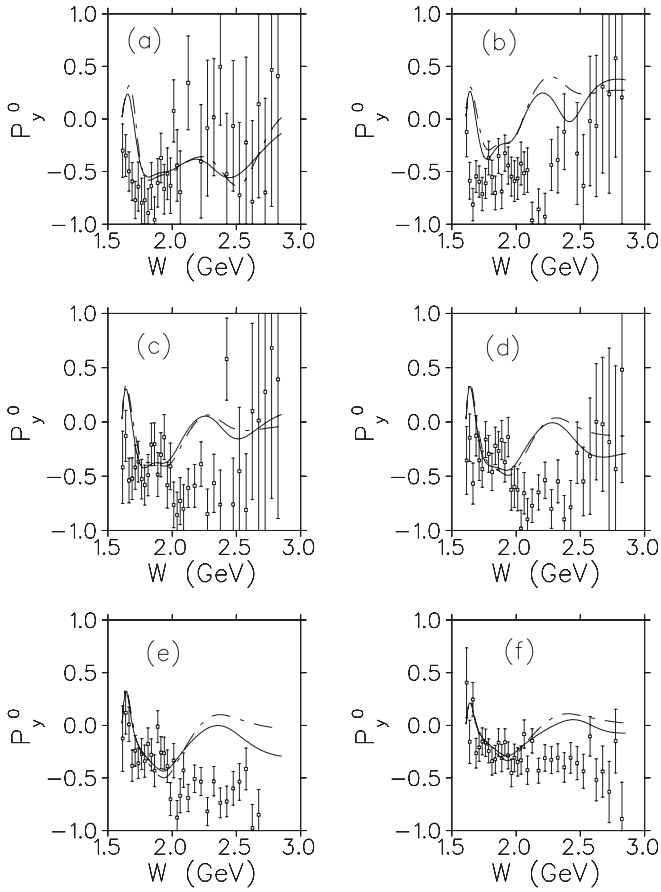


FIG. 9. $P_y^0$ vs $W$ for $E_{\rm Lab} = 5.499$ GeV, $-q^2 = 1.90$ GeV$^2$, and (a) $\cos\theta_K = -0.725$, (b) $\cos\theta_K = -0.217$, (c) $\cos\theta_K = 0.106$, (d) $\cos\theta_K = 0.305$, (e) $\cos\theta_K = 0.706$, (f) $\cos\theta_K = 0.910$. In each panel, the solid curve was obtained with the new fit and the dash-dotted curve with fit B as described in the text. All curves have been averaged over the angle $\phi$ as described in the text. Data are from Ref. [2].

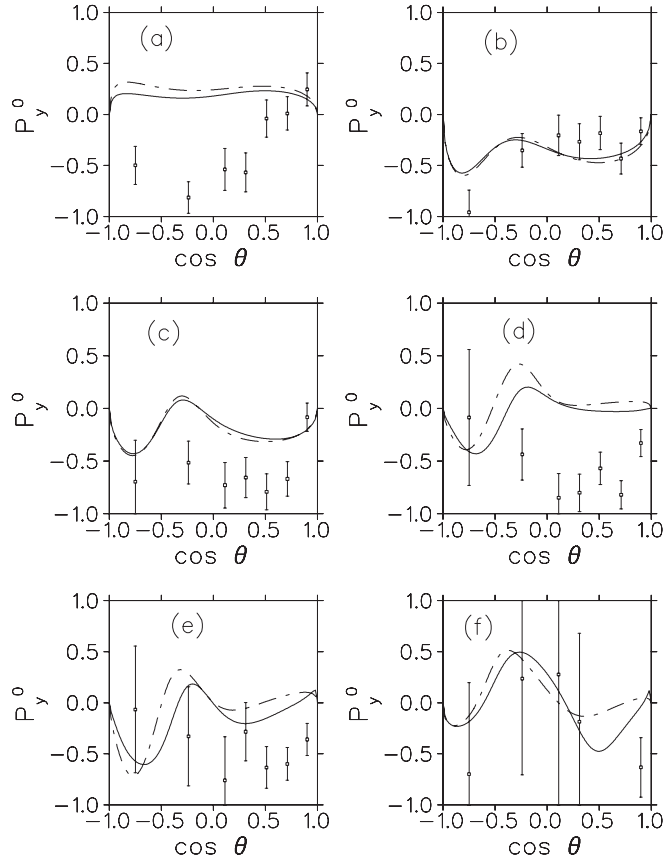


FIG. 10. $P_y^0$ vs $\cos\theta_K$ for $E_{\rm Lab} = 5.499$ GeV and (a) $W = 1.633$ GeV, $-q^2 = 2.11$ GeV$^2$, (b) $W = 1.863$ GeV, $-q^2 = 2.08$ GeV$^2$, (c) $W = 2.063$ GeV, $-q^2 = 2.01$ GeV$^2$, (d) $W = 2.274$ GeV, $-q^2 = 1.90$ GeV$^2$, (e) $W = 2.475$ GeV, $-q^2 = 1.75$ GeV$^2$, (f) $W = 2.724$ GeV, $-q^2 = 1.52$ GeV$^2$. In each panel, the solid curve was obtained with the new fit and the dash-dotted curve with fit B as described in the text. All curves have been averaged over the angle $\phi$ as described in the text. Data are from Ref. [2].

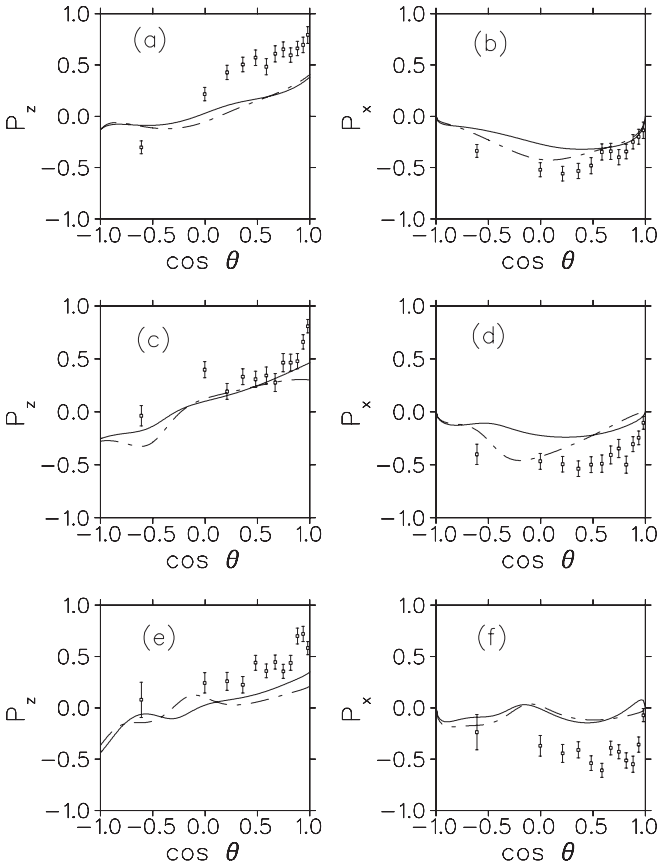


FIG. 11. $P_z'$ vs $\cos\theta_K$ for $E_{\rm Lab} = 5.754$ GeV and (a) $W = 1.753$ GeV, $-q^2 = 2.61$ GeV$^2$, (c) $W = 1.985$ GeV, $-q^2 = 2.56$ GeV$^2$, (e) $W = 2.314$ GeV, $-q^2 = 2.41$ GeV$^2$. $P_x'$ vs $\cos\theta_K$ for $E_{\rm Lab} = 5.754$ GeV and (b) $W = 1.753$ GeV, $-q^2 = 2.61$ GeV$^2$, (d) $W = 1.985$ GeV, $-q^2 = 2.56$ GeV$^2$, (f) $W = 2.314$ GeV, $-q^2 = 2.41$ GeV$^2$. In each panel, the solid curve was obtained with the new fit and the dash-dotted curve with fit B as described in the text. All curves have been averaged over the angle $\phi$ as described in the text. Data are from Ref. [1].

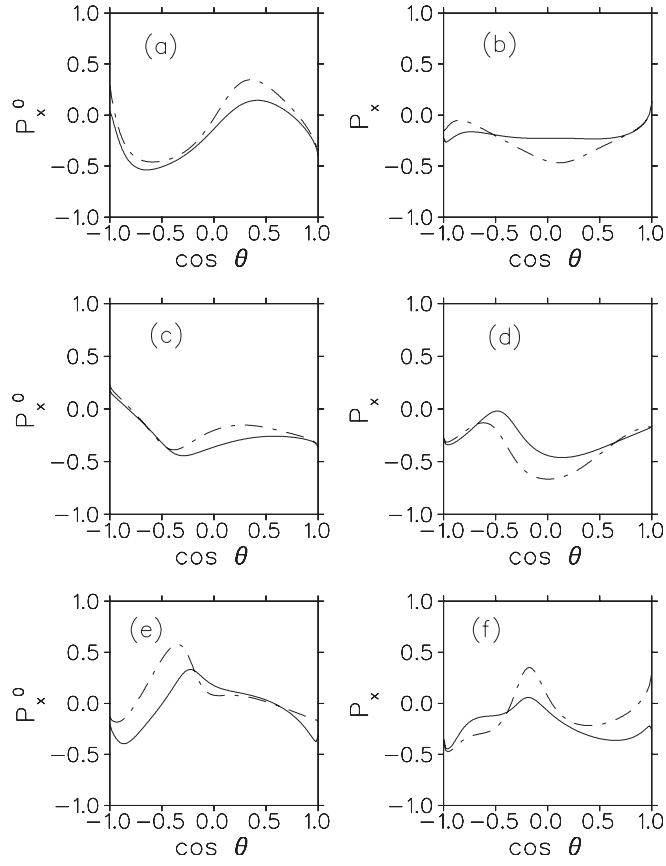


FIG. 12. $P_x^0$ vs $\cos\theta_K$ for $E_{\rm Lab} = 5.754$ GeV, $\phi = 30^\circ$, and (a) $W = 1.753$ GeV, $-q^2 = 2.61$ GeV$^2$, (c) $W = 1.985$ GeV, $-q^2 = 2.56$ GeV$^2$, (e) $W = 2.314$ GeV, $-q^2 = 2.41$ GeV$^2$. $P_x'$ vs $\cos\theta_K$ for $E_{\rm Lab} = 5.754$ GeV, $\phi = 30^\circ$, and (b) $W = 1.753$ GeV, $-q^2 = 2.61$ GeV$^2$, (d) $W = 1.985$ GeV, $-q^2 = 2.56$ GeV$^2$, (f) $W = 2.314$ GeV, $-q^2 = 2.41$ GeV$^2$. In each panel, the solid curve was obtained with the new fit and the dash-dotted curve with fit B as described in the text.

several values of $\cos\theta_K$. Here the similarity between the two fits is quite obvious. At low energy, the two fits yield nearly identical results; at higher energy, the new fit is somewhat better than fit B, but still does not reproduce the data very well between 2.1 and 2.5 GeV.

The angular distributions of the induced polarization asymmetry and the two transferred polarization asymmetries are displayed in Figs. 10 and 11 for various energies. Again, the two fits yield similar results, and although the new fit is slightly better than fit B at some of the energies shown, it does not significantly reduce the discrepancies with the data that were apparent in the results obtained with the previous fits.

Figures 12, 13, and 14 present results obtained with both the new fit and the previous fit B for the particular choice $\phi = 30^\circ$. As in the previous figures of this section, the solid curves correspond to the new fit and the dot-dashed curves to fit B. No data has been included in these figures since all of the data presently available represent averages over the angle $\phi$ and, as discussed previously, the calculated polarization asymmetries have a significant dependence on this angle. As for the $\phi$ averaged results, the results yielded by the fits for particular $\phi$ are quite similar, but there are some differences. At the higher energy values, the two transferred polarization asymmetries, $P_x'$ and $P_z'$, exhibit structures in the angular distributions obtained with one of the fits that are either not present or considerably reduced with the other fit.

## VI. SUMMARY AND CONCLUSIONS

In summary, new results have been presented for a set of induced and transferred polarization asymmetries that have been recently measured by the CLAS collaboration. To obtain these results, an effective Lagrangian model was employed that supplements the Born contributions with a variety of $s$-channel, $u$-channel, and $t$-channel resonant terms and which incorporates form factors at the electromagnetic vertices. Two sets of results have been presented. The first makes use of two previous fits that did not include the induced and transferred polarization asymmetries in the fitted data set. The second set is based on a new fit that does incorporate these polarization asymmetries in the data fitted.

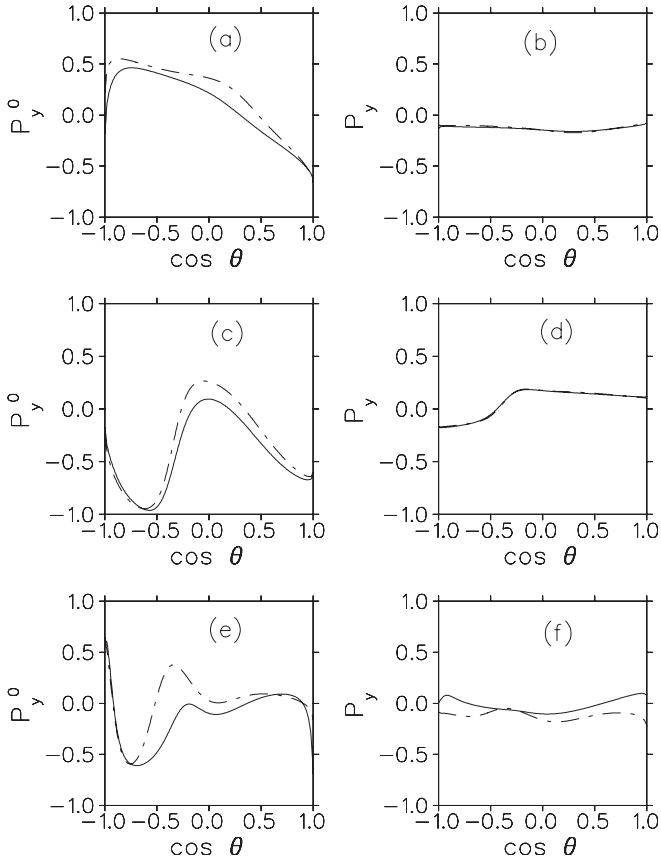


FIG. 13. $P_y^0$ vs $\cos\theta_K$ for $E_{\rm Lab} = 5.499$ GeV, $\phi = 30^\circ$, and (a) $W = 1.633$ GeV, $-q^2 = 2.11$ GeV$^2$, (c) $W = 2.063$ GeV, $-q^2 = 2.01$ GeV$^2$, (e) $W = 2.475$ GeV, $-q^2 = 1.75$ GeV$^2$. $P_y'$ vs $\cos\theta_K$ for $E_{\rm Lab} = 5.754$ GeV, $\phi = 30^\circ$, and (b) $W = 1.633$ GeV, $-q^2 = 2.11$ GeV$^2$, (d) $W = 2.063$ GeV, $-q^2 = 2.01$ GeV$^2$, (f) $W = 2.475$ GeV, $-q^2 = 1.75$ GeV$^2$. In each panel, the solid curve was obtained with the new fit and the dash-dotted curve with fit B as described in the text.

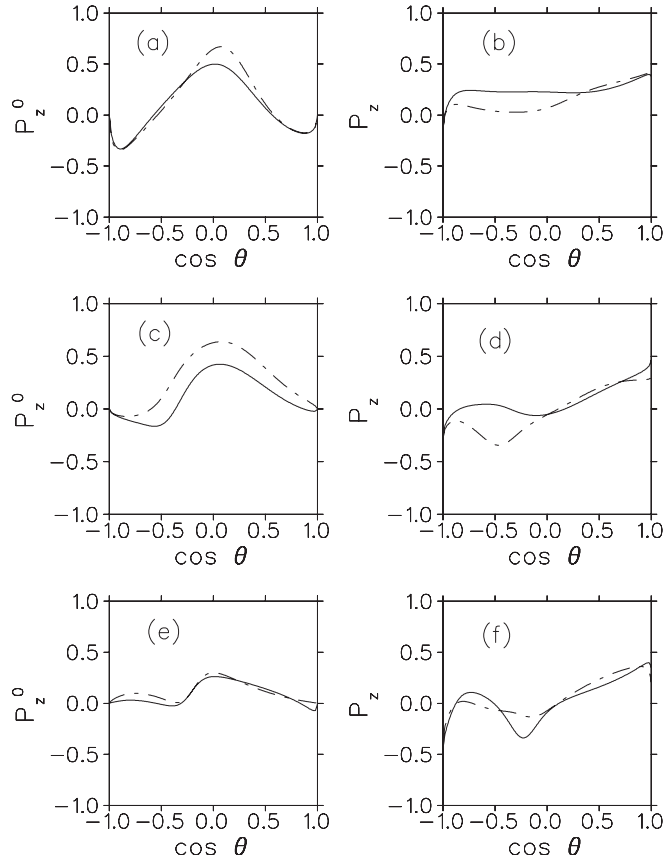


FIG. 14. $P_z^0$ vs $\cos\theta_K$ for $E_{\rm Lab} = 5.754$ GeV, $\phi = 30^\circ$, and (a) $W = 1.753$ GeV, $-q^2 = 2.61$ GeV$^2$, (c) $W = 1.985$ GeV, $-q^2 = 2.56$ GeV$^2$, (e) $W = 2.314$ GeV, $-q^2 = 2.41$ GeV$^2$. $P_z'$ vs $\cos\theta_K$ for $E_{\rm Lab} = 5.754$ GeV, $\phi = 30^\circ$, and (b) $W = 1.753$ GeV, $-q^2 = 2.61$ GeV$^2$, (d) $W = 1.985$ GeV, $-q^2 = 2.56$ GeV$^2$, (f) $W = 2.314$ GeV, $-q^2 = 2.41$ GeV$^2$. In each panel, the solid curve was obtained with the new fit and the dash-dotted curve with fit B as described in the text.

A number of issues were investigated that are connected with the the kinematic treatment of the data. These include the $q^2$ dependence of the observables, the sizes of the $\cos\theta_K$ bins, and the $\phi$ dependence of the data. The results obtained indicate that discrepancies between the calculations and the data cannot generally be attributed to differences in the handling of the kinematics. The only kinematic consideration in the handling of the data that seems to matter much is the treatment of the angle $\phi$, where results obtained after averaging over $\phi$ are significantly different from results obtained with a single value of $\phi$.

The two fits obtained previously yield rather different results for the induced polarization asymmetry $P_y^0$ in certain kinematic regions. By contrast, the results for the two transferred polarization asymmetries, $P_x'$ and $P_z'$, are much closer together. One interesting aspect of these results is the weakness of their $q^2$ dependence. This is significant because the virtual photoproduction observables should reduce to the values measured in real photoproduction as $q^2 \to 0$.

In comparison with the data, the model does fairly well in certain kinematic regions, but is not able to reproduce the data quantitatively over the whole kinematic range considered. In an attempt to improve the description of polarization asymmetries, a new fit was developed, which explicitly incorporates the polarization data in the fitted data set. Unfortunately, the resulting fit is quite similar to the previous fit B and does not significantly improve the model's reproduction of the polarization data. While this result may be partly attributable to large error bars, as mentioned previously, it is probably also due to shortcomings in the model, which, in common with most other models for the electromagnetic production of strangeness, may be missing important contributions to the underlying reaction mechanism.

Two directions suggest themselves for future work. One is to study various contributions to the model in greater detail with a view to uncovering relationships between particular trends in the data and particular contributions to the model. It might also be interesting to determine to what extent a reduced model with significantly fewer resonances can reproduce the results of the full model.

A second direction for future research is to extend the model to include $\Sigma^0$ production as well as $\Lambda$ production. $\Sigma^0$'s can be produced from intermediate $\Delta$ resonances in the $s$ channel and

thus involve contributions to the reaction mechanism that are not present in $\Lambda$ production. Moreover, while $\Lambda$ production data represents the bulk of the data from experiments studying the electroproduction of strangeness from the proton, there is now a significant amount of data for $\Sigma^0$ production both with real and virtual photons.


## ACKNOWLEDGMENTS

The author would like to acknowledge useful discussions with Dr. Brian Raue concerning the CEBAF polarization data and for providing access to the induced polarization asymmetry data prior to publication.



[1] D. S. Carmen *et al.*, Phys. Rev. Lett. **90**, 131804 (2003); Phys. Rev. C **79**, 065205 (2009).
[2] M. Gabrielyan *et al.*, arXiv:1406.4046.
[3] N. Levy, W. Majerotto, and B. J. Read, Nucl. Phys. B **55**, 493 (1973); **B55**, 513 (1973); A. Bartl and W. Majerotto, *ibid.* **B90**, 285 (1975).
[4] R. A. Adelseck, C. Bennhold, and L. E. Wright, Phys. Rev. C **32**, 1681 (1985); R. A. Adelseck and L. E. Wright, *ibid.* **38**, 1965 (1988); R. A. Adelseck and B. Saghai, *ibid.* **42**, 108 (1990).
[5] Robert A. Williams, Chueng-Ryon Ji, and Stephen R. Cotanch, Phys. Rev. C **46**, 1617 (1992).
[6] J. C. David, C. Fayard, G. H. Lamot, and B. Saghai, Phys. Rev. C **53**, 2613 (1996); T. Mizutani, C. Fayard, G.-H. Lamot, and B. Saghai, *ibid.* **58**, 75 (1998).
[7] T. Mart and C. Bennhold, Nucl. Phys. A **639**, 237c (1998).
[8] T. Mart, C. Bennhold, and C. E. Hyde-Wright, Phys. Rev. C **51**, R1074 (1995); H. Haberzettl, C. Bennhold, T. Mart, and T. Feuster, *ibid.* **58**, R40 (1998); T. Mart and C. Bennhold, *ibid.* **61**, 012201(R) (1999); H. Haberzettl, T. Mart, and C. Bennhold, Acta Physica Polonica B **31**, 2387 (2000); H. Haberzettl, C. Bennhold, and T. Mart, Nucl. Phys. A **684**, 475c (2001).
[9] S. Janssen, J. Ryckebusch, W. Van Nespen, D. Debruyne, and T. Van Cauteren, Eur. Phys. J. A **11**, 105 (2001); S. Janssen, J. Ryckebusch, D. Debruyne, and T. Van Cauteren, Phys. Rev. C **65**, 015201 (2001); S. Janssen, D. G. Ireland, and J. Ryckebusch, Phys. Lett. B **562**, 51 (2003); S. Janssen, J. Ryckebusch, and T. Van Cauteren, Phys. Rev. C **67**, 052201(R) (2003).
[10] Oren V. Maxwell, Phys. Rev. C **76**, 014621 (2007).
[11] M. Vanderhaeghen, M. Guidal, and J.-M. Laget, Phys. Rev. C **57**, 1454 (1998); M. Guidal, J.-M. Laget, and M. Vanderhaeghen, *ibid.* **61**, 025204 (2000); **68**, 058201 (2003).
[12] B. Borasoy, E. Marco, and S. Wetzel, Phys. Rev. C **66**, 055208 (2002); B. Borasoy, P. C. Bruns, U.-G. Meissner, and R. Nissler, *ibid.* **72**, 065201 (2005); Eur. Phys. J. A **34**, 161 (2007).
[13] B. Golli and S. Sirca, Eur. Phys. J. A **47**, 1 (2011).
[14] Oren V. Maxwell, Phys. Rev. C **86**, 064612 (2012).
[15] Oren V. Maxwell, Phys. Rev. C **85**, 034611 (2012).
[16] J. W. C. McNabb *et al.*, Phys. Rev. C **69**, 042201 (2004).
[17] R. Bradford *et al.*, Phys. Rev. C **73**, 035202 (2006).
[18] R. Bradford *et al.*, Phys. Rev. C **75**, 035205 (2007).
[19] M. Q. Tran *et al.*, Phys. Lett. B **445**, 20 (1998); S. Goers *et al.*, *ibid.* **B464**, 331 (1999); K. H. Glander *et al.*, Eur. Phys. J. A **19**, 251 (2004).
[20] R. G. T. Zegers *et al.*, Phys. Rev. Lett. **91**, 092001 (2003); M. Sumihama *et al.*, Phys. Rev. C **73**, 035214 (2006).
[21] A. Lleres *et al.*, Eur. Phys. J. A **31**, 79 (2007); A. D'Angelo *et al.*, *ibid.* **31**, 441 (2007).
[22] A. Lleres *et al.*, Eur. Phys. J. A **39**, 149 (2009).
[23] P. Ambrozewicz *et al.*, Phys. Rev. C **75**, 045203 (2007).
[24] R. Nasseripour *et al.*, Phys. Rev. C **77**, 065208 (2008).
[25] Alejandro de la Puente, Oren V. Maxwell, and Brian A. Raue, Phys. Rev. C **80**, 065205 (2009).